Detecting Fe(II) Spin-Crossover by Modulation of Appended Eu(III) Luminescence in a Single Molecule

Deorukhkar, Neel; Glaus, Charlotte; Guenee, Laure; Besnard, Céline; Piguet, Claude

How to cite

DEORUKHKAR, Neel et al. Detecting Fe(II) Spin-Crossover by Modulation of Appended Eu(III) Luminescence in a Single Molecule. In: Journal of the American Chemical Society, 2023, vol. 146, n° 1, p. 308–318. doi: 10.1021/jacs.3c09017

This publication URL: https://archive-ouverte.unige.ch/unige:174245
Publication DOI: 10.1021/jacs.3c09017

Publication: *J. Am. Chem. Soc.* **2024**, *146,* 308-318. DOI 10.1021/jacs.3c09017

Detecting Fe(II) Spin-Crossover by Modulation of Appended Eu(III) Luminescence in a Single Molecule.

Neel Deorukhkar[a], Charlotte Egger[a], Laure Guénée[b], Céline Besnard[b], and Claude Piguet[a,*]

[a] *Department of Inorganic and Analytical Chemistry. University of Geneva, 30 quai E. Ansermet CH-1211 Geneva 4, Switzerland*

[b] *Laboratory of Crystallography. University of Geneva, 24 quai E. Ansermet. CH-1211 Geneva 4, Switzerland*

[*]Email: Claude.Piguet@unige.ch

ABSTRACT: Multifunctionality in spin-crossover (SCO) devices is limited to macroscopic or nanoscopic materials because of the need for long-range effects for inducing favorable cooperativity, efficient energy migration processes and detectable magnetization transfer. The difficult reproducibility, control and rational design of doped materials let some place to SCO processes modulating the optical properties of neighboring luminescent probes in single molecules. We report here on the combination of a $[FeN_6]$ chromophore, the SCO temperature and absorption spectra of which have been tuned to induce unprecedented room-temperature modulation of Eu(III)-based line-like luminescence in the molecular triple-helical $[EuFe(\mathbf{L2})_3]^{5+}$ complex in solution.

Introduction

Bifunctional luminescent spin-crossover (SCO) materials have actively been studied since more than a decade[1-3] because the detection of a luminescence signal is more efficient and/or easy to implement than other techniques usually used in the SCO field (magnetometry, optical absorption, Mössbauer spectroscopy).[4-6] Luminescence, especially for the line-like and well-controlled emission of trivalent lanthanides,[7-9] can provide superior contrast and sensitivity for non-contact (remote) signal detection of SCO processes with high spatial and temporal resolution, as demonstrated for thermometers,[10,11] gas sensors[12,13] and photonic switches.[14-17] The crucial point for the latter bifunctionality considers

the rational modulation of the energy transfer rate constant $W_{D,A}$ between the luminescent probe, working as the donor (D), and the SCO iron partner acting as the acceptor (A). The associated Fermi golden rule (eq A1-1, Appendix 1),[18,19] which is pertinent to intermolecular energy transfers applied to doped macroscopic materials and nanoparticles,[20,21] can be indeed easily adapted to intramolecular processes limited to a single D-A entity as depicted in eq (1).[22,23]

$$W_{D,A}^{intra} = \frac{2\pi}{\hbar}\left|\left\langle \psi_{DA^*} \middle| H \middle| \psi_{D^*A} \right\rangle\right|^2 \Omega_{D,A} \quad (1)$$

H is the interaction Hamiltonian that mediates energy transfer from the excited donor D^* to the ground-state acceptor A, and $\Omega_{D,A}$ is the spectral overlap integral (eq 2) where $g_D(E)$ and $g_A(E)$ are the normalized line shape functions for the homogeneous lines of the donor (emission spectrum) and acceptor (absorption spectrum), respectively.[24,25]

$$\Omega_{D,A} = \int g_A(E) \cdot g_D(E) dE \quad (2)$$

$\Omega_{D,A}$ ensures energy conservation and intimately depends on the location of the excited states of the two partners implied in the energy transfer, while the matrix element, summarized as $\left|\left\langle DA^* \middle| H \middle| D^*A \right\rangle\right|^2$, relies on (i) the interaction mechanism (through-space electrostatic or double electron exchange) and (ii) the distance separating the donor (D) and the acceptor (A).[26-28] Consequently, in a rigid single D-A unit, the low-spin to high-spin transition operating in the [FeN_6] acceptor has limited effect on the latter matrix element, and modulation of the energy transfer rate constant $W_{D,A}^{intra}$ mainly depends on the variation of the spectral overlap integral $\Omega_{D,A}$ (eq 2).[23] The kinetics of low-spin Fe(HS) to high-spin Fe(II) relaxation in spin-crossover compounds can be described as non-adiabatic multi-phonon process in the strong coupling limit.[29] Interestingly, the thermal high-spin state shows the same increase of~0.2˚A in metal–ligand bond length as the light-induced high-spin state, and photo-induced spin-state conversion has been thus extensively used to monitor the intersystem crossing dynamics of spin-crossover complexes in solution.[30-35] For iron(II), it occurs on the microsecond timescale at around ambient temperature.[29] Under steady-state irradiation, the

absorption spectrum of the low-spin configuration in [FeN$_6$] chromophores is dominated by a broad and intense metal-to-ligand charge transfer band (MLCT) covering the visible part of the electromagnetic spectrum (purple trace in Figure 1). Much weaker, and usually masked spin-allowed d-d transitions ($^1T_1 \leftarrow {}^1A_1$ and $^1T_2 \leftarrow {}^1A_1$ in O_h symmetry) are expected within the same spectral domain. For the high-spin counterpart, the MLCT band is usually much less intense and shifted toward higher energy (orange trace in Figure 1), while a single weak ($10 \leq \varepsilon \leq 30$ M^{-1}·cm^{-1}) spin-allowed transition ($^5E \leftarrow {}^5T_2$ in O_h symmetry) occurs on the low-energy side (around 900 nm).[1,23,36]

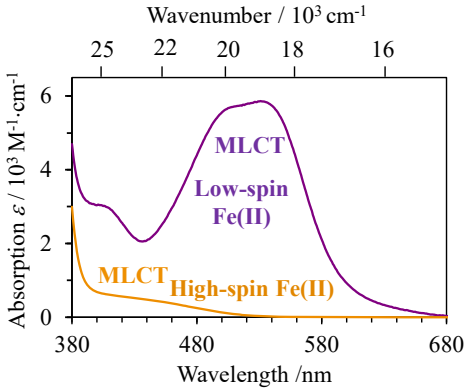

Figure 1. Room temperature electronic absorption spectra recorded for [Fe(II)N$_6$] chromophores in low-spin [LaFe(**L1**)$_3$]$^{5+}$ (purple trace) and in high-spin [LaFe(**L4**)$_3$]$^{5+}$ (orange trace) in acetonitrile. Numerical data taken from reference 36.

Taking the SCO-[FeN$_6$] chromophore as the acceptor, we foresee that the major changes in $\Omega_{D,A}$ required for modulating the global luminescent signal rely on the choice of a donor with an emission spectrum operating at low energy, i.e. below 19000 cm^{-1} (Figure 1), and with narrow electronic transitions. In this context, the use of the sharp and intense green Tb($^5D_4 \rightarrow {}^7F_5$) emission at 18350 cm^{-1} appeared to be successful for monitoring Fe(II) spin transitions in a [FeN$_6$]@SiO$_2$ nanorod materials statistically grafted with Tb(III) coordination complexes.[37] At the molecular level, a trinuclear [(Pt**L**)$_2$Fe]$^{6+}$ adduct has been designed for modulating Pt-based emission in the 18000-20000 cm^{-1} range, but the very similar photoluminescent properties recorded with, or without the Fe(II) center led to the conclusion that the Pt-based MLCT emission at 530 nm is practically not affected by the spin transition core ($W^{intra}_{Pt \rightarrow Fe} \approx 0$), and the failure of any luminescence modulation by

the appended SCO process (Figure 2a).[38] The heterometallic triple-stranded helicate $[EuFe(\mathbf{L1})_3]^{5+}$ led to the reverse situation where the intramolecular Eu→Fe energy transfers were so efficient, for both high-spin ($\eta^{ET}_{Eu\rightarrow HS\text{-}Fe}$ = 97.9%) and low-spin Fe(II) ($\eta^{ET}_{Eu\rightarrow LS\text{-}Fe}$ ≥ 99.9%), that only some faint residual Eu-based emission could be detected in the solid state at high temperature when HS-$[EuFe(\mathbf{L1})_3]^{5+}$ dominated the speciation (Figure 2b).[23]

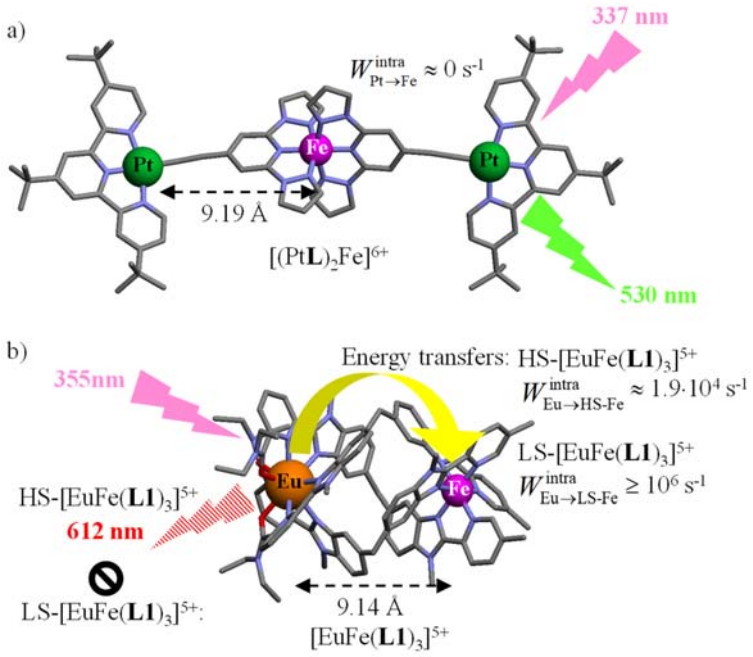

Figure 2. Attempts to modulate metal-based emission by an appended Fe(II) spin-crossover process in single molecular units as reported for a) $[(Pt\mathbf{L})_2Fe]^{6+}$ [31] and b) $[EuFe(\mathbf{L1})_3]^{5+}$.[23]

Overcoming the later limitation for the Eu-Fe pair found in $[EuFe(\mathbf{L1})_3]^{5+}$ with the ultimate goal of restoring significant and easily detectable Eu-based luminescence upon Fe(II) spin-state equilibrium around room temperature may consider separately, or altogether, the three following options. 1) The Eu···Fe distance should be extended to reduce the energy transfer rate constants while tuning $\left|\left\langle \psi_{DA^*} \left| H \right| \psi_{D^*A} \right\rangle\right|^2$ in eq (1) (a R^{-6} dependence is expected according to the through-space Förster mechanism).[24,28] 2) The emission spectrum of the donor should be shifted toward lower energy in order to decrease the spectral overlap integral $\Omega_{D,A}$. The replacement of Eu(III) with Nd(III) or Yb(III) emitters could be considered to match this requirement. 3) The nature of the heterocyclic

nitrogen atoms bound to Fe(II) should be adapted to shift the spin crossover temperature $T_{1/2}$, i.e. the temperature at which 50% of both high-spin and low spin forms coexist, toward lower values (eq 3).[39] This will maximize the mole fraction of less absorbing high-spin species at high temperature, while a concomitant drift of the Fe-MLCT bands toward higher energy could further reduce $\Omega_{D,A}$.

$$Fe^{II}_{low\text{-}spin} \underset{}{\overset{K_{SCO}}{\rightleftharpoons}} Fe^{II}_{high\text{-}spin} \qquad -RT\ln(K_{SCO}) = \Delta H_{SCO} - T\Delta S_{SCO} \text{ and } T_{1/2} = \frac{\Delta H_{SCO}}{\Delta S_{SCO}} \qquad (3)$$

The first option requires a tricky extension of the triple helix,[40] the second option would limit detection in the NIR which is much less attractive for non-specialists. The third option is explored in this contribution despite the inherent difficulty produced by the partial enthalpy/entropy (*H*/*S*) compensation[41-43] established for SCO processes[44] which limits any major drift in the transition temperature since $T_{1/2} = \Delta H_{SCO}/\Delta S_{SCO}$ (eq 3).[45].

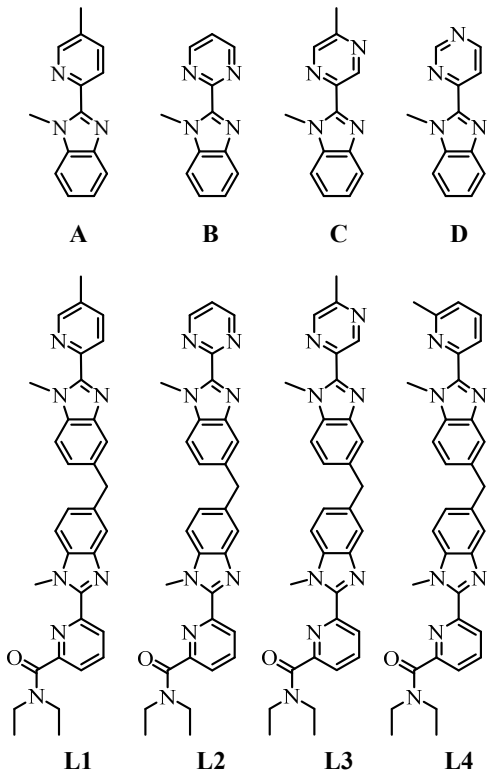

Scheme 1. Chemical structures of the model didentate **A**-**D** binding units and their related introduction into the segmental didentate-tridentate ligands **L1**-**L4**.

For the didentate N∩N units bound to Fe(II) (**L** = **A**-**D** in Scheme 1), taken as models for the terminal binding site in the related triple helices $[EuFe(\mathbf{L}\boldsymbol{k})_3]^{5+}$, a linear correlation $\Delta H_{SCO} = \alpha \cdot \Delta S_{SCO} + \beta$ could be established for the mononuclear $[Fe(\mathbf{L})_3]^{2+}$ series with α = 601(103) K and β = -24936(9020) J·mol^{-1}.[39] Since $\alpha > 0$ (*H*/*S* compensation) and $\beta < 0$ (strong-cohesion regime),[45] any planned shift of the transition temperature toward lower values in CD_3CN, $T_{1/2} = \Delta H_{SCO}/\Delta S_{SCO} = \alpha + (\beta/\Delta S_{SCO})$, requires smaller ΔS_{SCO} values (and consequently ΔH_{SCO}) and finally weaker Fe-N bond affinities. The hydrolysis-sensitive 1-methyl-2-(pyrimidin-2-yl)-1H-benzo[d]imidazole binding unit (**B**) appeared to be the best candidate for weakening the Fe-N bond while maintaining SCO transitions at accessible temperature in solution.[39] We show in this contribution that the latter didentate binding unit can be introduced into the segmental ligand **L2** to ultimately produce the stable dinuclear self-assembled $[EuFe(\mathbf{L2})_3]^{5+}$ helicate, for which a rare modulation of Eu(III) luminescence by SCO Fe(II) operating in a single molecule is demonstrated in solution.

Results and Discussion

Synthesis and molecular structures of ligand L2 and of the self-assembled triple-stranded helicates $[LnM(L2)_3]^{5+}$ (Ln = La, Nd, Eu; M = Fe, Zn). Contrary to **L1**[46] and **L4**,[36] for which the hydrolysis-resistant methylpyridine unit could be connected to the diphenylmethane spacer as the first step of the synthetic strategy, the introduction of pyrazine as found in **L3**,[47] or of more reactive pyrimidines as found in precursors **B** or **D** must occur during the last synthetic steps in order to avoid decomposition. With this in mind, the non-symmetrical ortho-nitro amine **3** was prepared in six steps (Scheme A2-1)[47] and used as the nucleophile for connecting the terminal pyrimidine unit **2** via an amide bond in **4** (Scheme 2). The subsequent reduction/cyclization step leading to the final ligand **L2** must avoid any traces of acids, which are incompatible with the maintenance of the pyrimidine unit, but especially useful for catalyzing the ultimate benzimidazole cyclization.[48] The best strategy in our hands used a reduction of **4** with sodium dithionite in ethanol/water followed by cyclization using microwave heating under pressure to give a 46% yield of ligand **L2**. The ESI-MS spectrum (Figure

S1) and elemental analysis (Appendix 2) support the formation of the segmental ligand **L2**, in complete agreement with its ^{1}H NMR spectrum, which points to fast rotations around the interannular C(benzimidazole)-C(pyrimidine) bond. An [A_2X] spin system is observed for the protons of the pyrimidine (Figure S2) leading to an average C_s-symmetry for **L2**, which is further supported by the [A_2] spin system displayed by the central methylene spacer (Figure S3). In its crystalline form (Tables S1-S2, Figure S4), **L2** adopts a roughly planar conformation of the connected aromatic rings, in which both *N*-methyl substituents are oriented on the same side of the methylene spacer (Figure 3).

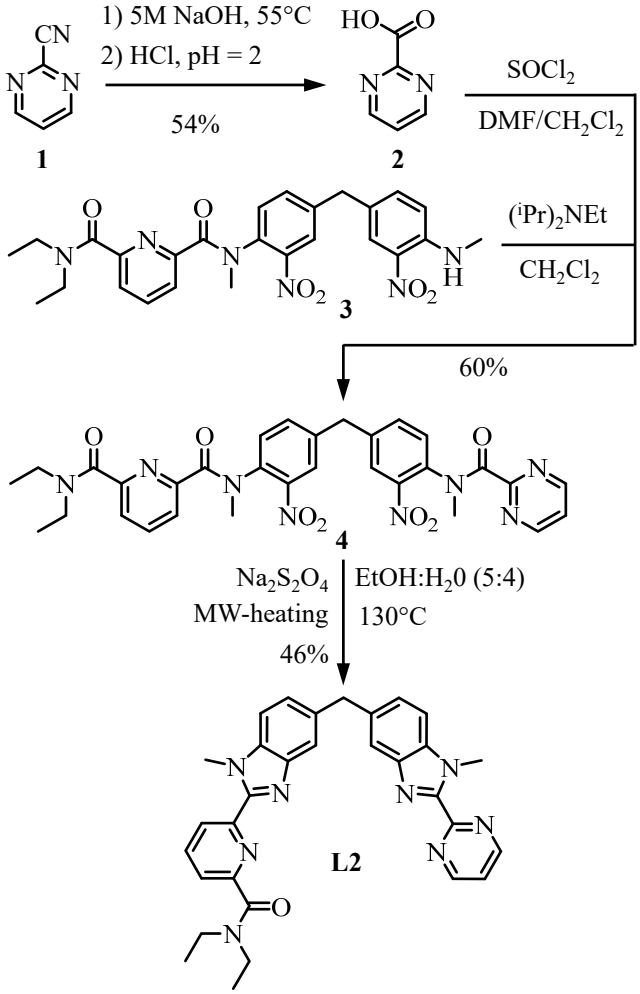

Scheme 2. Synthetic strategy for the preparation of the segmental ligand **L2**.

As previously detailed for **L1**[46] and **L3**[49], the stoichiometric mixing of $Ln(CF_3SO_3)_3$ (1.0 eq, Ln = La, Nd, Eu), $M(CF_3SO_3)_2$ (1.0 eq, M = Fe, Zn) and **L2** (3.0 eq) in CD_3CN at total millimolar concentrations results in the fast (< 1 minute) and selective assembly of a single $[LnM(\mathbf{L2})_3]^{5+}$

complex with C_3-symmetry (eq 4, Figure S5), which can be evidenced in solution by the combination of (i) ESI-MS spectra, which are dominated by the detection of gas-phase $[LnM(\mathbf{L2})_3(CF_3SO_3)_n]^{(5-n)+}$ adducts (n = 0-3, Figures S6-S11), and (ii) ^{1}H NMR spectra (Figure S12).

$$Ln^{3+} + M^{2+} + 3\ \mathbf{L2} \rightleftarrows [LnM(\mathbf{L2})_3]^{5+} \qquad \beta_{1,1,3}^{Ln,M,\mathbf{L2}} = \frac{\left|LnM(\mathbf{L2})_3\right|}{\left|Ln\right|\left|M\right|\left|\mathbf{L2}\right|^3} \qquad (4)$$

The wrapping of the ligand around the three-fold axis is responsible for the [AB] spin system recorded for the diastereotopic methylene protons (loss of the symmetry plane) and for the 2.0 ppm upfield shift of the protons k and o in the final $[LaZn(\mathbf{L2})_3]^{5+}$ complex (Figure S12a), which is diagnostic for a twisted conformation of the diphenylmethane spacer (Figure 3). Furthermore, the coordination of Zn(II) at the didentate site introduces an inequivalence between the pyrimidine protons q and s, owing to the loss of the time-averaged symmetry plane bisecting the bound pyrimidine unit. Coordination of La(III) at the tridentate site is evidenced by a 0.35 ppm downfield shift of the pyridine-proton f signal (Figure S12). According that stability constants in the range $28 \leq \log\left(\beta_{1,1,3}^{Ln,Zn,\mathbf{L1}}\right) \leq 29$ [46] and $24 \leq \log\left(\beta_{1,1,3}^{Ln,Fe,\mathbf{L1'}}\right) \leq 25$ [50] were previously reported for equilibrium (4), no significant decomplexation is expected for concentrations larger than the micromolar domain for the analogous $[LnM(\mathbf{L2})_3]^{5+}$ helicates. This is fully confirmed in the submillimolar range by the observed invariance of both ^{1}H NMR spectra for $[LaZn(\mathbf{L2})_3]^{5+}$ (Figure S12b), and electronic absorption spectra for $[LaFe(\mathbf{L2})_3]^{5+}$ (Figure S13) upon dilution. We can therefore safely conclude that the triple helicates $[LnM(\mathbf{L2})_3]^{5+}$ correspond to > 99% of the speciation in the millimolar acetonitrile solutions used for studying magnetic and photophysical properties (see next sections).

Stoichiometric reactions of 3 eq of the ligand **L2** with 1 eq of $Zn(CF_3SO_3)_2$ or $Fe(CF_3SO_3)_2$ and 1 eq $La(CF_3SO_3)_3$ or $Nd(CF_3SO_3)_3$ or $Eu(CF_3SO_3)_3$ in acetonitrile yielded microcrystalline powders of the respective complexes upon diffusion of diethylether or ^{t}butyl-methylether (Appendix 2 and Table A2-1). The powders, when redissolved in acetonitrile and allowed to crystallize by (very) slow diffusion of either diethylether or ^{t}butyl-methylether yielded single crystals suitable for characterization by X-ray diffraction at 120 K for $[EuZn(\mathbf{L2})_3](CF_3SO_3)_5 \cdot 1.5CH_3CN \cdot 0.625C_5H_{12}O$,

$[NdZn(\mathbf{L2})_3](CF_3SO_3)_5\cdot 1.5CH_3CN$, $[LaFe(\mathbf{L2})_3](CF_3SO_3)_5\cdot 2.5CH_3CN\cdot 0.5C_5H_{12}O$, $[EuFe(\mathbf{L2})_3](CF_3SO_3)_5\cdot 2.5CH_3CN\cdot 0.5C_5H_{12}O$, and $[NdFe(\mathbf{L2})_3](CF_3SO_3)_5\cdot 2CH_3CN\cdot 0.5C_4H_{10}O$ (Table 1 and Figure 3; Tables S3-S14, Figures S14-S18). In absence of satisfying single crystals, a microcrystalline powder of $[LaZn(\mathbf{L2})_3](CF_3SO_3)_5$ was analyzed by powder-XRD and gave a pattern that could be well indexed and refined with a similar cell to those of the other dinuclear helicates (Table 1; Figures S19-S20).

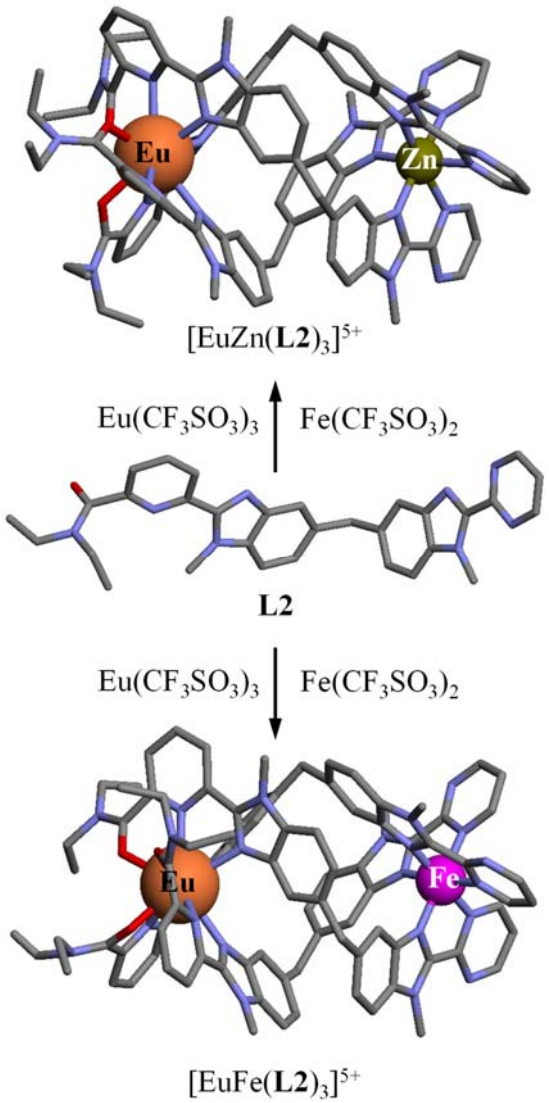

Figure 3. Molecular structures of the ligand **L2** and the cationic triple-stranded helicates $[EuZn(\mathbf{L2})_3]^{5+}$ and $[EuFe(\mathbf{L2})_3]^{5+}$ as observed in the crystal structures of **L2**, $[EuZn(\mathbf{L2})_3](CF_3SO_3)_5\cdot 1.5CH_3CN\cdot 0.625C_5H_{12}O$ and $[EuFe(\mathbf{L2})_3](CF_3SO_3)_5\cdot 2.5CH_3CN\cdot 0.5C_5H_{12}O$ measured at 120K.

Table 1. Structural data for the complexes of **L2** in the solid-state at 120 K.

	$[EuZn(\mathbf{L2})_3](CF_3SO_3)_5$	$[NdZn(\mathbf{L2})_3](CF_3SO_3)_5$	$[LaFe(\mathbf{L2})_3](CF_3SO_3)_5$	$[EuFe(\mathbf{L2})_3](CF_3SO_3)_5$	$[NdFe(\mathbf{L2})_3](CF_3SO_3)_5$
Crystal System	Monoclinic	Monoclinic	Monoclinic	Monoclinic	Monoclinic
d (M-N_{bz})[a]	2.096(27)	2.098(34)	1.978(5)	1.976(3)	1.976(3)
d (M-N_{py})[a]	2.21(4)	2.212(34)	1.981(5)	1.981(5)	1.982(11)
α / ° [a]	8.66(3.85)	8.5(3.8)	9.26(3.88)	9.19(3.59)	8.61(4.47)
β / ° [a]	85.96(1.79)	87.13(4.27)	86.56(3.26)	86.27(3.42)	86.54(3.09)
γ / ° [a]	76.83(49)	76.58(78)	81.01(15)	81.37(40)	80.96(24)
Octahedron[b]	1.411	1.475	0.668	0.676	0.680
Trigonal prism[b]	14.151	13.921	15.421	15.244	15.320
d (Ln-N_{bz})[c]	2.570(13)	2.608(4)	2.668(9)	2.574(12)	2.611(12)
d (Ln-N_{py})[c]	2.578(13)	2.608(17)	2.684(13)	2.584(8)	2.616(17)
d (Ln-O)[c]	2.406(18)	2.450(17)	2.488(17)	2.401(21)	2.439(23)
Muffin[d]	1.772	1.978	2.193	1.869	1.961
Spherical capped square antiprism[d]	1.802	1.968	2.261	1.901	1.980
Bond valence sum[e]	3.07	3.11	3.15	3.06	3.12
d (Ln-M)	9.144(1)	9.158(1)	9.2703(6)	9.253(1)	9.254(1)

[a] Didentate binding unit with d-block-metal with (α) Interannular intraligand angles, (β) Interchelate Angles (Fig. S23) and (γ) Chelate Bite Angles [b] SHAPE scores[52,53] as compared to an ideal octahedron or trigonal prism at the didentate site. [c] Tridentate binding unit with f-block-metal. [d] SHAPE scores[52,53] as compared to muffin geometry or spherical square capped antiprism at the tridentate site (Fig. S22). Shape 2.1 can be downloaded free at https://www.ee.ub.edu/downloads/. [e] Bond valence sum for the lanthanide coordinated at the tridentate binding sites.[51]

A rapid look at the molecular structures show (very) similar triple-stranded dinuclear arrangements for all the isolated $[LnM(\mathbf{L2})_3]^{5+}$ cations (Figure 3 and Figure S21) with intermetallic separations around 9.2 Å (Table 1). Focusing on the Zn(II)···Eu(III) distance leads to 9.144(1) Å in $[EuZn(\mathbf{L2})_3]^{5+}$, which is marginally longer than those previously reported for the isostructural $[EuZn(\mathbf{L1})_3]^{5+}$ (8.45 Å)[23] and $[EuZn(\mathbf{L3})_3]^{5+}$ (8.5 Å) complexes.[49] A detailed structural analysis (Appendix 3)[51] points to very similar low-symmetry nine-coordinate $[LnN_6O_3]$ chromophores for Ln = La, Nd, Eu reminiscent of muffins or of spherical capped square antiprisms, as quantified by a SHAPE analysis (Table 1 entries 11-12 and Figure S22).[52,53] Focusing on the $[MN_6]$ unit reveals pseudo-octahedral geometries, which are more distorted around the spherical Zn^{2+} than around the low-spin Fe^{2+} at 120 K, a cation which is known to display large ligand-field stabilization energies in octahedral geometry (Table 1, entry 6).[54] To summarize, the dinuclear $[LnM(\mathbf{L2})_3]^{5+}$ complexes are highly stable in acetonitrile solution and the helical mold produced by the three wrapped ligands is flexible enough to provide similar molecular structures whatever the cations used for the self-assembly process (Ln = La, Nd, Eu and M = Fe, Zn).

Spin state equilibria of $[LnFe(L2)_3]^{5+}$ in solution (Ln = La, Nd, Eu). The evolution of the magnetic susceptibilities (χ_M^{tot} in $cm^3 \cdot mol^{-1}$) for the self-assembled complexes in solution were achieved through Evans' method (eq A1-2, Appendix 1).[55] The measurement of the diamagnetic complex $[LaZn(\mathbf{L2})_3]^{5+}$ provides $\chi_M^{tot}([LaZn]) = \chi_M^{dia}$, from which the searched pure paramagnetic contribution $\chi_M^{para}(Fe)$ assigned to the Fe(II) spin-state equilibrium in $[LaFe(\mathbf{L2})_3]^{5+}$ can be obtained with eq (5) after considering the solvent correction[56] and the associated change in the density of the solvent (red disks in Figure 4).[57,58] In eq (5), $\Delta\nu$ is the chemical shift (in Hz) measured between the two signals of a reference indicator simultaneously placed in the studied solution containing the complex at a concentration c (in $g \cdot cm^{-3}$) and in an isolated coaxial tube in absence of complex, and M is the molecular mass of the complex (in $g \cdot mol^{-1}$).

$$\chi_{\mathrm{M}}^{\mathrm{para}}(\mathrm{Fe}) = \chi_{\mathrm{M}}^{\mathrm{tot}}([\mathrm{LaFe}]) - \chi_{\mathrm{M}}^{\mathrm{dia}}([\mathrm{LaZn}]) = \frac{1}{v_{\mathrm{o}} S_{\mathrm{f}}}\left(\frac{\Delta\nu^{\mathrm{LaFe}} M^{\mathrm{LaFe}}}{c^{\mathrm{LaFe}}} - \frac{\Delta\nu^{\mathrm{LaZn}} M^{\mathrm{LaZn}}}{c^{\mathrm{LaZn}}}\right) \quad (5)$$

In $[\mathrm{NdFe}(\mathbf{L2})_3]^{5+}$ and $[\mathrm{EuFe}(\mathbf{L2})_3]^{5+}$, the paramagnetic lanthanide partners display negligible intramolecular isotropic magnetic coupling constant with the remote high-spin Fe(II) (> 9Å),[36] and their $[\mathrm{LnN_6O_3}]$ coordination spheres are almost identical to those observed in $[\mathrm{NdZn}(\mathbf{L2})_3]^{5+}$ and $[\mathrm{EuZn}(\mathbf{L2})_3]^{5+}$. With this in mind, the paramagnetic contribution $\chi_{\mathrm{M}}^{\mathrm{para}}(\mathrm{Fe})$ assigned to the Fe(II) spin-state equilibrium in the latter dinuclear helicates can be simply deduced from the differences $\chi_{\mathrm{M}}^{\mathrm{para}}(\mathrm{Fe}) = \chi_{\mathrm{M}}^{\mathrm{tot}}([\mathrm{LnFe}]) - \chi_{\mathrm{M}}^{\mathrm{tot}}([\mathrm{LnZn}])$ and plotted in Figure 4 (green and blue disks, see Appendix 4 for details).

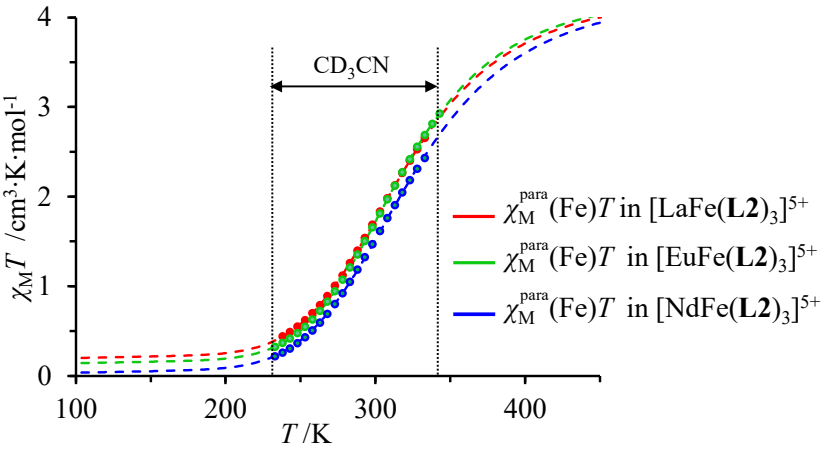

Figure 4. Plot of experimental molar Fe(II) paramagnetic susceptibility ($\chi_{\mathrm{M}}^{\mathrm{para}}(\mathrm{Fe})\cdot T$) *versus* temperature ($T$) for a 10 mM solution of the $[\mathrm{LnFe}(\mathbf{L5})_3]^{5+}$ complexes in CD_3CN (disks). The dashed curves represent $\chi_{\mathrm{M}}^{\mathrm{para}}(\mathrm{Fe})\cdot T$ computed with eq (8) and using the fitted values of ΔH_{sco} and ΔS_{sco} for individual SCO processes (Table 2).

Once experimental $\chi_{\mathrm{M}}^{\mathrm{para}}(\mathrm{Fe})\cdot T$ at different temperatures are at hand for the complexes $[\mathrm{LnFe}(\mathbf{L2})_3]^{5+}$, their strict assignment to the spin-state equilibrium (3) allows us to extract the associated thermodynamic parameters ΔH_{SCO} and ΔS_{SCO} (Table 2) by non-linear least-squares fits with eq (6) while using the Curie constants C_{hs} and C_{ls} for high-spin, respectively low-spin Fe(II) in solution and the temperature independent susceptibilities (TIP) previously found for the mononuclear

analogue $[Fe(\mathbf{B})_3]^{2+}$ in solution (C_{hs} = 4.10(3) $cm^3 \cdot K \cdot mol^{-1}$, TIP_{hs} = 369(3) x 10^{-6} $cm^3 \cdot mol^{-1}$, C_{hs} = 0.0 $cm^3 \cdot K \cdot mol^{-1}$, TIP_{hs} = 342(3) x 10^{-6} $cm^3 \cdot mol^{-1}$, see Appendix 5 for details).[39]

$$\chi_M^{para}(Fe)T = \frac{\left(C_{ls} - C_{hs} + T(TIP_{ls} - TIP_{hs})\right)}{\left[1 + e^{\left(-\frac{\Delta H_{SCO}}{RT} + \frac{\Delta S_{SCO}}{R}\right)}\right]} + C_{hs} + T \cdot TIP_{hs} \quad (6)$$

Slightly better fits could be obtained with eq (A1-3), which considers the possibility of some minor oxidation of Fe(II) into Fe(III) (mole fraction $x_{Fe(III)} \leq 0.03$, see details in Appendix 5), but they do not significantly alter the global thermodynamic parameters.

Table 2. Thermodynamic constants (ΔH_{sco}, ΔS_{sco}), transition temperatures ($T_{1/2}$) for $[LnFe(\mathbf{L}\boldsymbol{k})_3]^{5+}$ in CD_3CN (**L*k*** = **L1**, **L2**, **L3**).

Complex	ΔH_{sco} /kJ·mol^{-1}	ΔS_{sco} /J·mol^{-1}·K^{-1}	$T_{1/2}$ /K	Reference
$[LaFe(\mathbf{L1})_3]^{5+}$	29.6(2)	86.2(5)	344(3)	46
$[LaFe(\mathbf{L4})_3]^{5+}$	37.9(5)	92(1)	412(8)	46
$[LaFe(\mathbf{L2})_3]^{5+}$	23.5(1)	74.2(1)	317(2)	This work
$[NdFe(\mathbf{L2})_3]^{5+}$	23.1(1)	71.8(1)	322(2)	This work
$[EuFe(\mathbf{L2})_3]^{5+}$	24.3(1)	76.7(1)	317(1)	This work

The transition temperatures 317 ≤ $T_{1/2}$ ≤ 322 observed for $[LnFe(\mathbf{L2})_3]^{5+}$ (Table 2, column 4) are in good agreement with $T_{1/2}$ = 309(6) K reported for the mononuclear model complex *fac*-$[Fe(\mathbf{B})_3]^{2+}$ in CD_3CN solution.[39] It is not surprising that $T_{1/2}$ is slightly higher for the same C_3-symmetrical $[Fe(N\cap N')_3]^{2+}$ chromophore in the dinuclear $[LnFe(\mathbf{L2})_3]^{5+}$ complexes since the expansion of the $[Fe(II)N_6]$ sphere concomitant with the spin transition process is slightly affected by the minor constraints exerted by the coordinated Ln(III) neighbor through the helicate scaffold.[59] In line with our strategy,[39] the transition temperature of the spin crossover process for isolated molecules in solution stepwise indeed decreases in going from 2-benzimidazole-pyrazine ($T_{1/2}([LaFe(\mathbf{L4})_3]^{5+})$ = 412 K) to 2-benzimidazole-pyridine ($T_{1/2}([LaFe(\mathbf{L1})_3]^{5+})$ = 344 K) and, finally, 2-benzimidazole-

pyrimidine ($T_{1/2}$([LaFe(**L2**)$_3$]$^{5+}$) = 317 K) didentate binding units. This makes [EuFe(**L2**)$_3$]$^{5+}$ the most promising candidate for the experimental demonstration that the modulation of Eu(III) luminescence by Fe(II)-SCO can be implemented into isolated molecules in solution, a phenomenon previously reported for [EuFe(**L1**)$_3$](CF$_3$SO$_3$)$_5$ in the solid state[23] and for doped materials.[1,37]

In the solid state, intermolecular interactions prevent simple molecular-based rationalization and complicated multivariate are required to partially analyze the crucial influence of long-range effects resulting from crystal packing.[60] Both [LaFe(**L2**)$_3$](CF$_3$SO$_3$)$_5$·1.45H$_2$O (ΔH_{SCO} = 13.4(5) kJ·mol^{-1}, ΔS_{SCO} = 33.0(1) J·mol^{-1}·K^{-1}, $T_{1/2}$ = 406(2) K, cooperativity index γ = 3.76(1) kJ·mol^{-1}) and [EuFe(**L2**)$_3$](CF$_3$SO$_3$)$_5$·1.85H$_2$O (ΔH_{SCO} = 23.2(2) kJ·mol^{-1}, ΔS_{SCO} = 54.4(4) J·mol^{-1}·K^{-1}, $T_{1/2}$ = 427(4) K, cooperativity index γ = 2.99(1) kJ·mol^{-1}) exhibit spin crossover transitions with transition temperatures $T_{1/2}$ larger than those found in solution (Table A6-1 in Appendix 6).

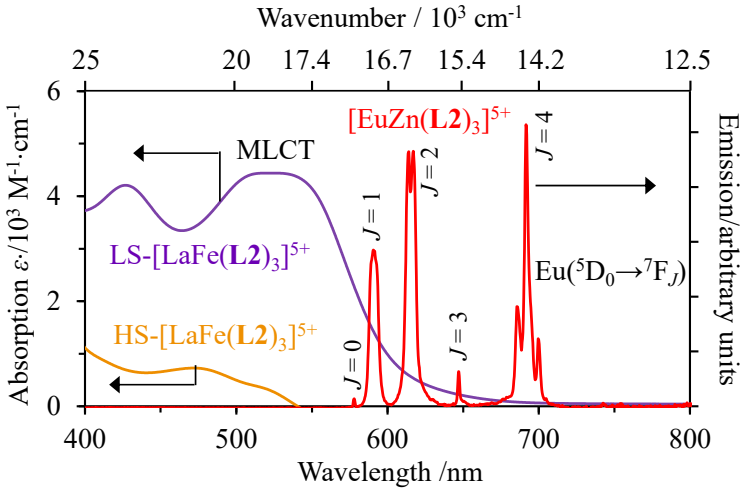

Figure 5. Deconvoluted absorption spectra of high-spin and low-spin [LaFe(**L2**)$_3$]$^{5+}$ (left part) and emission spectra (λ_{exc} = 331 nm) of [EuZn(**L2**)$_3$]$^{5+}$ in acetonitrile.

Having ΔH_{SCO} and ΔS_{SCO} in solution, the associated spin state equilibrium constant K_{SCO} is deduced with eq (3), from which the mole fraction of high-spin Fe(II), $x_{hs} = K_{SCO}/(1+K_{SCO})$, is accessible at any temperature. Consequently, the record of variable temperature absorption spectra for [LaFe(**L2**)$_3$]$^{5+}$ at 1.66 mM concentration in acetonitrile (Figure S24, negligible decomplexation

according to eq 4) is controlled by the spin-state equilibrium, from which the decadic temperature-independent molar absorption coefficients of each contributing complex, i.e. high-spin HS-[LaFe(**L2**)$_3$]$^{5+}$ ($\varepsilon_{hs}^{\lambda}$) and low-spin LS-[LaFe(**L2**)$_3$]$^{5+}$ ($\varepsilon_{ls}^{\lambda}$), can be deduced by a multi-linear square fit using eq (A1-4).[49] The deconvoluted visible absorption spectrum of LS-[LaFe(**L2**)$_3$]$^{5+}$ (purple trace in Figure 5) shows MLCT transitions rather similar to those recorded for LS-[LaFe(**L1**)$_3$]$^{5+}$ (Figure 1),[49] but slightly red-shifted with lower molar extinction coefficients (Figure S25). The MLCT transition in HS-[LaFe(**L2**)$_3$]$^{5+}$ is of much lower intensity and centered at λ_{max} = 472 nm (orange trace in Figure 5). The 30% reduction of the extinction coefficient of the MLCT transitions in going from 2-benzimidazole-pyridine in LS-[LaFe(**L1**)$_3$]$^{5+}$ (Figure 1) to 2-benzimidazole-pyrimidine in LS-[LaFe(**L2**)$_3$]$^{5+}$ (Figure 5) is especially fortuitous for restraining the intramolecular Eu(III)$\rightarrow$Fe(II)$_{LS}$ transfer in [EuFe(**L2**)$_3$]$^{5+}$ (decrease of the overlap integral in eq 2) and thus limiting the quenching of Eu-centered emission in solution.[21]

Modulation of Eu-based luminescence upon Fe(II) spin crossover operating in the molecular [EuFe(L2)$_3$]$^{5+}$ complex in solution. The binding of the ligands **L2** to M(II) (M = Fe, Zn) and Ln(III) (Ln = La, Eu) to form the triple helical complexes [LnM(**L2**)$_3$]$^{5+}$ in acetonitrile requires a *transoïd* to *cisoïd* rearrangement at both didentate and tridentate donor sites (Figure 3), which is accompanied by the expected[61,62] 1500 cm^{-1} red shift of the ligand-based spin-allowed $^1\pi_2^*\leftarrow{}^1\pi$ transitions in the absorption spectra (Figure 6). While the [LnZn(**L2**)$_3$]$^{5+}$ complexes are colorless, the Fe(II) analogues [LnFe(**L2**)$_3$]$^{5+}$ exhibit a purple-red color in their low-spin state and an orange-yellow color in the high-spin state produced by their specific MLCT absorptions, which cover the visible part of the electromagnetic spectrum (Figure 5). Upon UV ligand-based excitation, a related red shift is detected in the associated $^1\pi_2^*\rightarrow{}^1\pi$ fluorescence emission spectra in going from **L2** (Figures S26-S27) to [LaM(**L2**)$_3$]$^{5+}$ (Figures S28-S29), while the weaker $^3\pi^*\rightarrow{}^1\pi$ phosphorescence, which covers the 500-600 nm range for both ligand and complexes, can be detected only at low temperature (Figures S30-S31).

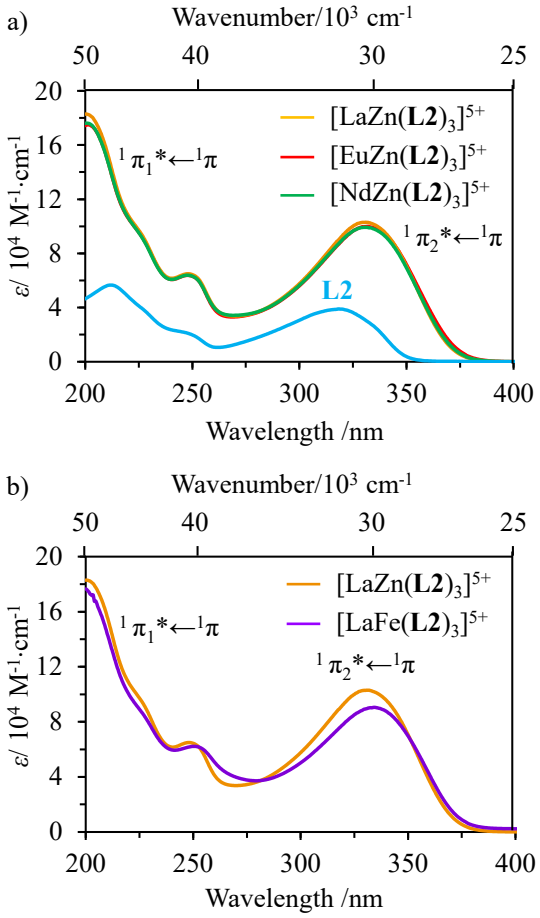

Figure 6. Absorption spectra of a) **L2** and $[LnZn(\mathbf{L2})_3]^{5+}$ complexes (Ln= La, Eu, Nd) and b) $[LaM(\mathbf{L2})_3]^{5+}$ (M = Fe, Zn) in ~1 mM acetonitrile solutions.

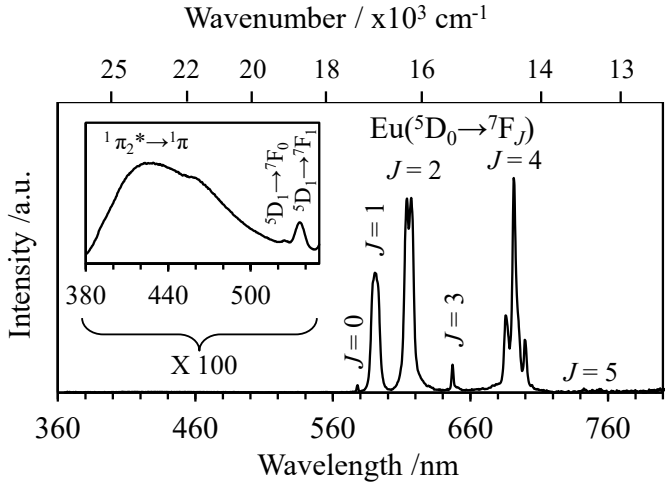

Figure 7. Emission spectrum of $[EuZn(\mathbf{L2})_3]^{5+}$ (λ_{exc} = 331 nm) dominated by the Eu($^5D_0 \rightarrow {}^7F_J$) emission bands (~1mM solution in acetonitrile).

For $[EuZn(\mathbf{L2})_3]^{5+}$, ligand-centered excitation at 331 nm (30210 cm^{-1}) reveals intense Eu(III)-based $^5D_0 \rightarrow {}^7F_J$ emission bands (J = 0-4), which result from indirect sensitization through efficient **L2**-to-Eu(III) energy transfers (*antenna effect*),[63,64] a mechanism almost quantitative as ascertained by the detection of only residual ligand-based $^1\pi_2^* \rightarrow {}^1\pi$ fluorescence (Figure 7). Variable temperature emission spectra recorded for a solution of $[EuZn(\mathbf{L2})_3]^{5+}$ (λ_{exc} = 335 nm, Figure S32) show a decrease in intensity of the Eu($^5D_0 \rightarrow {}^7F_J$) transitions with increasing temperature, due to the concomitant increase of the relaxation rate constant $k_{Eu}^{relax} = 1/\tau_{Eu}^{relax}$ affecting the Eu($^5D_0$) excited state (red markers in Figure 8, Table S15 and Figure S33). The decay rate constants of the excited Eu($^5D_0$) spectroscopic level can be partitioned between radiative and non-radiative contributions $k_{Eu}^{relax} = k_{Eu}^{rad} + k_{Eu}^{non\text{-}rad}$. In the case of transitions that are electron-dipole forbidden, but are made partially allowed by coupling to the lattice that induce off-parity crystal field components, as it is the case for 4f→4f transitions, the radiative rate constant k_{Eu}^{rad} exhibits temperature dependence summarized in eq (7),[65] where k^0 is the radiative rate constant at T = 0 K obeying Einstein's relationship for spontaneous emission,[66] $h\nu$ represents the coupling phonon mode and k_B is Boltzmann's constant.

$$k_{Eu}^{rad} = k^0 \coth\left(h\nu / 2k_B T\right) \qquad (7)$$

Since an average phonon bath of $h\nu \approx 2000$ cm^{-1} is representative for the available coupling phonon mode in lanthanide coordination complexes,[67] eq (7) thus predicts a maximum drift of 3% for k_{Eu}^{rad} in the 230-330 K range. This could be confirmed in the emissive $[EuZn(\mathbf{L2})_3]^{5+}$ complex, because the $^5D_0 \rightarrow {}^7F_1$ transition corresponds to an allowed magnetic dipole transition with no contribution from induced electric dipole components. Since magnetic dipole transitions in lanthanide ions are practically independent of the ion's surroundings, the spontaneous emission probability for the magnetic dipole transition in Eu(III) can be well calculated by theory to give $A_{0\text{-}1}$ = 14.65 s^{-1}.[68] Application of eq (A1-5)[69] to the variable temperature steady-state emission spectra recorded for

$[EuZn(\mathbf{L2})_3]^{5+}$ (Figure S32) indeed returned a roughly constant value of $k_{Eu}^{rad} \approx 190\ s^{-1}$ within the 230-330 K range accessible in acetonitrile (Figure S34).

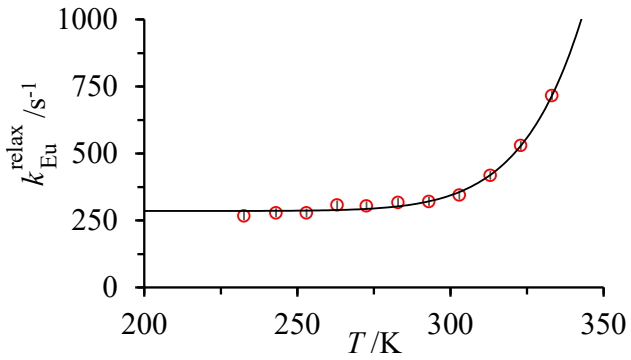

Figure 8. Plot of experimental total decay rate constants $k_{Eu}^{relax} = 1/\tau_{Eu}^{relax}$ for Eu($^5D_0$) in $[EuZn(\mathbf{L2})_3]^{5+}$ (red circles) *vs* temperature (T) in acetonitrile (λ_{exc} = 355 nm). The black trace represents the non-linear least-squares fit using eq (9).

On the other side, $k_{Eu}^{non\text{-}rad}$ is modeled with an Arrhenius-type temperature-dependent non-radiative phonon-assisted deactivation (eq 8), in which $k_{Eu}^{non\text{-}rad,0}$ stands for the non-radiative relaxation at $T \rightarrow \infty$ and $E_{Eu}^{non\text{-}rad}$ is the activation energy of the phonon-assisted relaxation pathway (in kJ/mol). The low-temperature tunneling, being much smaller than the radiative decay, is neglected.[23,24,67]

$$k_{Eu}^{non\text{-}rad} = k_{Eu}^{non\text{-}rad,0} \cdot \exp\left(-\frac{E_{Eu}^{non\text{-}rad}}{RT}\right) \quad (8)$$

Altogether, the combination of eq (8) for $k_{Eu}^{non\text{-}rad}$ with a temperature-independent radiative rate constant k_{Eu}^{rad} gives eq (9), which was used for fitting the experimental data with the help of non-linear least squares techniques (black trace in Figure 8).

$$k_{Eu}^{relax} = k_{Eu}^{rad} + k_{Eu}^{non\text{-}rad} = k_{Eu}^{rad} + k_{Eu}^{non\text{-}rad,0} \cdot \exp\left(-\frac{E_{Eu}^{non\text{-}rad}}{RT}\right) \quad (9)$$

The fitted radiative relaxation rate constant amounts to k_{Eu}^{rad} = 285(1) s^{-1} (or $\tau_{Eu}^{rad} = 1/k_{Eu}^{rad}$ = 3.50(5) ms). It is in good agreement with τ_{rad} = 2.89(2) ms measured previously for the analogous $[EuZn(\mathbf{L1})_3]^{5+}$ triple-helicate,[23] and lies in the range obtained from the integration of the emission

spectra with eq (A1-5) ($k_{Eu}^{rad} \approx 190$ s^{-1}; Figure S33). The non-radiative relaxation is characterized by $k_{Eu}^{non\text{-}rad,0} = 3.16(1)\cdot 10^{10}$ s^{-1} and $E_{Eu}^{non\text{-}rad} = 50.2(1)$ kJ.mol^{-1}, which is larger than 39.4(6) kJ.mol^{-1} reported for $[EuZn(\mathbf{L1})_3]^{5+}$.[23]

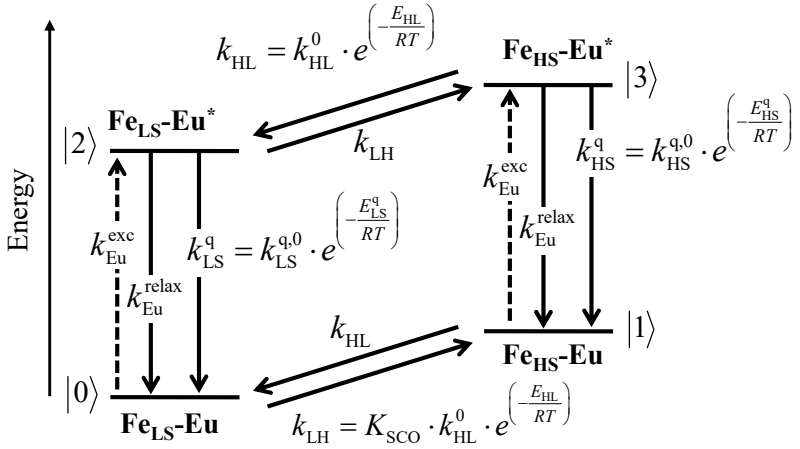

Scheme 3. Kinetic scheme for the luminescent monitoring of the Fe(II) spin-state using Eu(III) in the dinuclear $[EuFe(\mathbf{L2})_3]^{5+}$ complex. Dashed upward arrows = excitation, full downward arrows = relaxation and straight diagonal arrows = low-spin ↔ high-spin transformations (Adapted from ref 23).

Upon replacement of Zn(II) with Fe(II) in $[EuFe(\mathbf{L2})_3]^{5+}$, the absorption spectrum of the $[FeN_6]$ acceptor covers the visible part of the electromagnetic spectrum and, depending on the Fe(II) spin state, variable spectral overlap integral $\Omega_{D,A}$ are expected with the emission spectrum of the $[EuN_6O_3]$ chromophore (Figure 5). This opens two novel routes for quenching Eu($^5D_0$)-centered luminescence via intramolecular Eu→Fe energy transfer (eq 1) modeled with eqs (A1-6)-(A1-7) for low-spin (k_{LS}^{q}), respectively high-spin (k_{HS}^{q}) Fe(II) (Scheme 3).[23] Altogether, the complete kinetic mechanism summarized in Scheme 3 combines the Fe(II) spin-crossover behavior modeled with k_{HL} (eq A1-8) and k_{LH} (eq A1-9), which are the first-order rate constants for low-spin→high-spin and high-spin→low-spin transitions, with its consequences on the searched population densities of the excited states $N^{|2\rangle}$ and $N^{|3\rangle}$ (labelled as Eu* in Scheme 3).

Beyond k_{Eu}^{relax} (eq 9), taken for [EuZn(**L2**)$_3$]$^{5+}$, and k_{LS}^{q}, k_{HS}^{q} discussed above, the steady-state population of Eu* (i.e. $N_{S\text{-}S}^{|2\rangle} + N_{S\text{-}S}^{|3\rangle}$) is further affected by the continuous excitation process k_{Eu}^{exc} given in eq (10) (dashed arrows in Scheme 3),[70] where λ_P is the pump wavelength, P is the incident pump intensity (W·cm^{-2}), h is the Planck constant, c is the speed of light in vacuum and σ_{Eu} is the absorption cross section ($\sigma^{i\to j} = 3.8\cdot10^{-21}\varepsilon^{i\to j}$).[66] Please note that, in molecular [EuFe(**L2**)$_3$]$^{5+}$ cations, indirect sensitization is obtained via absorption through the ligand-centered excited states followed by energy transfer onto the Eu(III) center (antenna effect). This justifies the neglect of stimulated emission processes in the associated kinetic Scheme 3.

$$k_{Eu}^{exc} = \frac{\lambda_P}{hc} P \sigma_{Eu} \tag{10}$$

Under the weak continuous excitation P = 8.1 mW·cm^{-2} of the Xenon lamp at λ_{exc} = 333 nm, the calculated (eq 10) pumping rate for [EuFe(**L2**)$_3$]$^{5+}$ amounts to only k_{exc}^{Eu}= 5.29 s^{-1} (ε = 102547 M^{-1}·cm^{-1}, σ = 3.89·10^{-16} cm^2), which implies that the steady-state excited-state population densities $N_{S\text{-}S}^{|2\rangle}$ and $N_{S\text{-}S}^{|3\rangle}$ are negligible compared with ground-state population densities. The following approximations hold $\frac{N_{S\text{-}S}^{|1\rangle}}{N_{S\text{-}S}^{|0\rangle}} \approx \frac{N_0^{|1\rangle}}{N_0^{|0\rangle}} = \frac{k_{LH}}{k_{HL}} = K_{SCO} = \exp\left(-\frac{\Delta G_{SCO}^0}{RT}\right)$ and $N_{S\text{-}S}^{|0\rangle} + N_{S\text{-}S}^{|1\rangle} = N_0$. The total emitted intensity $I_{S\text{-}S}$ under steady-state excitation is then given in eq (11) (see Appendix 7 for its derivation with $k_A = k_{LH} + k_{Eu}^{relax} + k_{LS}^{q}$ and $k_B = k_{HL} + k_{Eu}^{relax} + k_{HS}^{q}$).[23]

$$I_{S\text{-}S} = k_{Eu}^{rad}\left(N_{S\text{-}S}^{|2\rangle} + N_{S\text{-}S}^{|3\rangle}\right) = N_0 k_{Eu}^{exc} k_{Eu}^{rad}\left(\frac{k_{LH}\left(k_A + k_{HL}\right) + k_{HL}\left(k_B + k_{LH}\right)}{\left(k_{HL} + k_{LH}\right)\left(k_A k_B - k_{HL} k_{LH}\right)}\right) \tag{11}$$

Experimentally, one first notes that variable temperature excitation of [EuFe(**L2**)$_3$]$^{5+}$ in acetonitrile at 333 nm ($\tilde{\nu}$ = 30000 cm^{-1}) displays measurable Eu(^{5}D$_0\to{}^7$F$_J$) emission signals within the 233-333 K range (Figure 9a), a behavior which drastically contrasts with the lack of detectable emission previously reported for [EuFe(**L1**)$_3$]$^{5+}$ in solution.[23] The shift of the transition temperature $T_{1/2}$ by

circa 30 degrees in going from [EuFe(**L1**)$_3$]$^{5+}$ to [EuFe(**L2**)$_3$]$^{5+}$ (Table 1), combined with the very limited overlap between the Eu-emission spectrum and the HS-Fe(II) absorption spectrum in the latter complex (Figure 5), limits intramolecular Eu→Fe energy transfers to such an extent that radiative Eu-based emission (k_{Eu}^{rad}) becomes competitive with the non-radiative processes in solution (k_{Eu}^{relax}, k_{LS}^{q} and k_{HS}^{q} in Scheme 3).

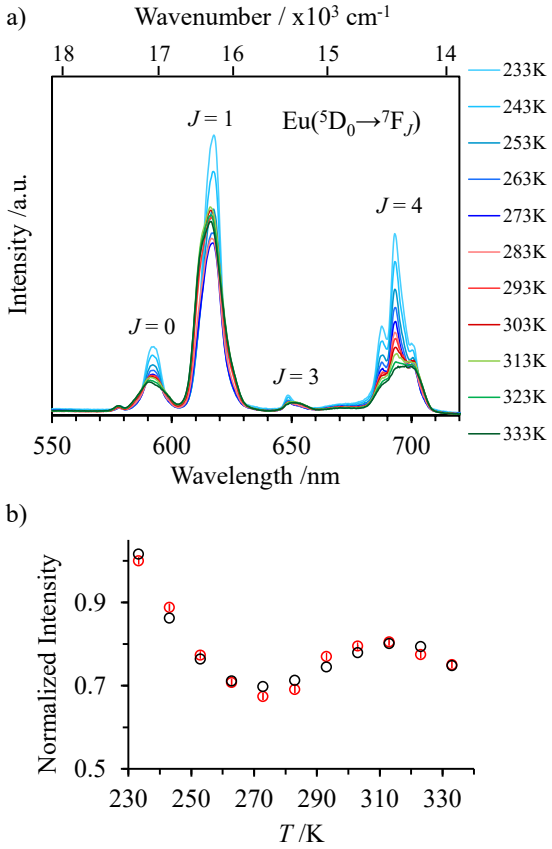

Figure 9. a) Variable temperature steady-state emission spectrum of [EuFe(**L2**)$_3$]$^{5+}$ (λ_{exc} = 333 nm, ~1 mM solution in acetonitrile) highlighting the variation in the intensity of the Eu($^5D_0 \rightarrow {}^7F_J$) emission bands. b) Normalized total integrated intensity ($I/I_{max}= I_T/I_{233K}$) for the emission of Eu(III) (red circles) in [EuFe(**L2**)$_3$]$^{5+}$ (λ_{exc} = 333 nm) in acetonitrile. The black circles represent the non-linear least squares fitted intensities computed with eq (11) and using the values collected in Table 3 column 5 (AF = 0.00048).

The temperature-dependent total emission intensity (red circles in Figure 9b) display an initial decline (230-270 K) due to the increase of the non-radiative vibrational relaxation processes *via* $k_{Eu}^{non\text{-}rad}$ (eq

8, Figure S33b), which is overcome within the 270-310 K range by the replacement of active quenching LS-Fe(II) centers with less efficient HS-Fe(II) acceptors according to the thermally-induced spin state equilibrium. At temperatures higher than 310 K, $k_{Eu}^{non\text{-}rad}$ dominates again the temperature dependence, and the total emitted intensity decreases. The resulting wavy trend experimentally observed for Eu($^5D_0 \rightarrow {}^7F_J$) in an acetonitrile solution of [EuFe(**L2**)$_3$]$^{5+}$ is unique for isolated single molecules (Figure 9b). For the parent complex [EuFe(**L1**)$_3$]$^{5+}$, the latter wavy emitted intensities could be only theoretically predicted because of the too large values of k_{LS}^{q} and k_{HS}^{q}.[23] The larger temperature range (10-400 K) accessible for [EuFe(**L1**)$_3$](CF$_3$SO$_3$)$_5$ in the solid state made the predicted modulation of the Eu(III)-centered emission partially attainable,[23] a trend which has been recently confirmed for a mononuclear spin crossover Fe(II) complex bearing peripheral naphthalene light emitters.[71]

A delicate non-linear least-square fit of the normalized experimental Eu(III)-centered emission in [EuFe(**L2**)$_3$]$^{5+}$ (I/I_{max} shown as red circles in Figure 9b) with eq (11) finally provided a satisfying undulating dependence of the emitted intensity on the temperature (black circles in Figure 9b) rebuilt with the fitted rate constants collected in Table 3 (see Scheme 3 and Appendix 8 for details). In order to limit the number of fitted parameters: (i) the relaxation of Eu(III), k_{Eu}^{relax}, observed and modelled with eq (9) for [EuZn(**L2**)$_3$]$^{5+}$ in acetonitrile were taken as pertinent for [EuFe(**L2**)$_3$]$^{5+}$ and (ii) k_{LH} and its Arrhenius dependence were deduced from k_{HL} and K_{SCO} (eq A1-9). The close-to-negligible values of k_{HS}^{q} (eq A1-7) within the 230-330 K (Table 3, entries 4-5) contributes for less than 1% of the total relaxation of Eu($^5D_0$) (Figure S35), which confirms the lack of measurable spectral overlap between the Eu((III) emission spectrum (580-750 nm, red trace in Figure 5) and the weak HS-Fe(II) absorption spectrum (450-540 nm, orange trace in Figure 5). The situation changes for k_{LS}^{q} (eq A1-6) which is responsible for more than 80% of the relaxation of the Eu($^5D_0$) excited state within the 240-330 K range accessible in acetonitrile. k_{Eu}^{relax} (eq 9) takes care of the missing 16-20% (Figure S35).

The opposite mirror bowl-shaped variations of both contributions ($\%k_{LS}^{q}$ and $\%k_{Eu}^{relax}$, Figure S35) are responsible for the wavy modulation of the Eu($^5D_0$)-centered light emission measured for [EuFe(**L2**)$_3$]$^{5+}$ in solution (Figure 9).

Table 3. Rate constants and activation energy barriers computed for the relaxation processes and spin crossover process depicted in Scheme 3 for [EuZn(**L2**)$_3$]$^{5+}$, [EuFe(**L2**)$_3$]$^{5+}$, [EuZn(**L1**)$_3$]$^{5+}$ and HS-[EuFe(**L4**)$_3$]$^{5+}$ in acetonitrile.

	[EuZn(**L1**)$_3$]$^{5+}$	[EuFe(**L4**)$_3$]$^{5+}$	[EuZn(**L2**)$_3$]$^{5+}$	[EuFe(**L2**)$_3$]$^{5+}$
k_{rad} /s^{-1}	339(2)	339(2) [a]	285(1)	285(1) [b]
$k_{non\text{-}rad}^{0}$ /s^{-1}	8(2)·10^8	8(2)·10^8 [a]	3.16(1)·10^{10}	3.16(1)·10^{10} [b]
$E_{Eu}^{non\text{-}rad}$ /kJ·mol^{-1}	39.4(6)	39.4(6) [a]	50.2(1)	50.2(1) [b]
$k_{HS}^{q,0}$ /s^{-1}	-	8(1)·10^6	-	8.85(1) s^{-1}
E_{HS}^{q} /kJ·mol^{-1}	-	14.7(4)	-	2.56(1)
$k_{LS}^{q,0}$ /s^{-1}	-	-	-	8.95(1)·10^5
E_{LS}^{q} /kJ·mol^{-1}	-	-	-	12.67(2)
k_{HL}^{0} /s^{-1}	-	-	-	1.63(1)·10^3
E_{HL} /kJ·mol^{-1}	-	-	-	1.49(1)
k_{LH}^{0} /s^{-1}	-	-	-	1.53(1)·10^7 [c]
E_{LH} /kJ·mol^{-1}	-	-	-	25.6(2) [c]
Reference	23	23	This work	This work

[a] Measured for [EuZn(**L1**)$_3$]$^{5+}$. [b] Measured for [EuZn(**L2**)$_3$]$^{5+}$. [c] Estimated from values of k_{HL}^{0} and E_{HL} found from the fit for [EuFe(**L2**)$_3$]$^{5+}$ using eq (A1-9).

Finally, the efficiency of the Eu(III)→LS-Fe(II) energy transfers is different for each specific Eu($^5D_0$→^7F_J) transitions because their specific spectral overlap integral $\Omega_{D,A}$ with the absorption spectrum of LS-Fe(II) varies. From Figure 5, one can immediately predicts that the spin-state equilibrium will weakly affects the intensity of the Eu($^5D_0$→$^7F_4$) emission band, whereas Eu($^5D_0$→$^7F_2$) will be the most sensitive one (Figure 10).

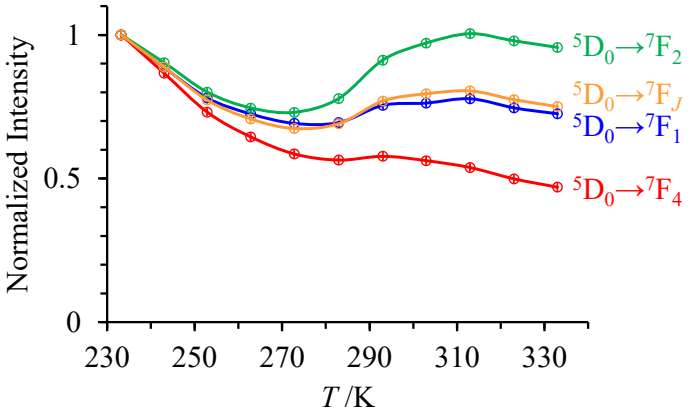

Figure 10. Normalized integrated intensities for the $^5D_0 \rightarrow {}^7F_1$ (blue trace), the $^5D_0 \rightarrow {}^7F_2$ (green trace), and the $^5D_0 \rightarrow {}^7F_4$ (red trace) emission bands, as a function of temperature for $[EuFe(\mathbf{L2})_3]^{5+}$ (λ_{exc} = 333 nm) in acetonitrile. The orange trace represents the total integrated intensity of Eu(III) against temperature.

Conclusion

The risky replacement of terminal pyridine in **L1** with hydrolysis-sensitive pyrimidine in **L2** could be only justified by the weaker Fe-N interactions resulting from the complexation of the didentate 1-methyl-2-(pyrimidin-2-yl)-1*H*-benzo[*d*]imidazole (**B**) binding unit with Fe(II), while maintaining (i) ligand-field strength compatible with SCO processes and (ii) thermodynamic stabilities compatible with the formation of close-to-quantitative pseudo-octahedral $[Fe(N^{\frown}N)_3]$ building blocks at millimolar concentrations.[39] As a rational consequence of the enthalpy/entropy compensation (strong cohesion regime) characterizing spin-state equilibria with $[FeN_6]$ chromophores, the transition temperature $T_{1/2}$ =317 K in $[EuFe(\mathbf{L2})_3]^{5+}$ becomes low enough to allow reasonable conversion of low-spin Fe(II) into high-spin Fe(II) within the temperature range accessible in acetonitrile. On the other hand, the unexpected, but favorable decrease of the intensity of both HS-Fe(II) and LS-Fe(II) MLCT absorption bands reduces significantly the quenching of the Eu($^5D_0$)-centered light emission by the adjacent Fe(II) site in $[EuFe(\mathbf{L2})_3]^{5+}$, which leads to what we believe to be the first experimental demonstration of the lanthanide-based emission detection of Fe(II)-SCO process operating in a single molecule in solution. The theoretical analysis of the mechanism of luminescence

modulation depicted in Scheme 3 is currently supported only by the analysis of the variation of the steady-state emission as a function of the temperature (eq 11), which leaves some debatable points concerning the kinetic aspects of the Fe(II) spin-state equilibrium. An access to additional information *via* the time-dependent Eu($^5D_0$) relaxation obtained under pulsed excitation in $[EuFe(\mathbf{L2})_3]^{5+}$ is complicated by the weak emission intensity $I_{Eu}(t)$ and the very short lifetimes expected for the biexponential decays (eqs A9-19 in Appendix 9). This delicate challenge is currently under investigation in our laboratory for further refining the origin of the intensity modulation reported in this work.

ASSOCIATED CONTENT

Supporting Information

The Supporting Information is available free of charge at https://pubs.acs.org/doi/XXX.
Complete experimental details, ligands and complexes characterizations, thermodynamic analysis, kinetic analysis and photophysical data (PDF).
X-ray data for **L2,** $[EuZn(\mathbf{L2})_3](CF_3SO_3)_5\cdot1.5CH_3CN\cdot0.625C_5H_{12}O$, $[NdZn(\mathbf{L2})_3](CF_3SO_3)_5\cdot1.5CH_3CN$, $[LaFe(\mathbf{L2})_3](CF_3SO_3)_5\cdot2.5CH_3CN\cdot0.5C_5H_{12}O$, $[EuFe(\mathbf{L2})_3](CF_3SO_3)_5\cdot2.5CH_3CN\cdot0.5C_5H_{12}O$ and $[NdFe(\mathbf{L2})_3](CF_3SO_3)5\cdot0.5C_4H_{10}O\cdot2CH_3CN$ (CIF).

AUTHOR INFORMATION

Corresponding Author

Claude Piguet - *Department of Inorganic and Analytical Chemistry. University of Geneva, 30 quai E. Ansermet CH-1211 Geneva 4 (Switzerland)*; *orcid.org/0000-0001-7064-8548*
Email: Claude.Piguet@unige.ch

Authors

Neel Deorukhkar - *Department of Inorganic and Analytical Chemistry. University of Geneva, 30 quai E. Ansermet CH-1211 Geneva 4 (Switzerland)*.

Charlotte Egger - *Department of Inorganic and Analytical Chemistry. University of Geneva, 30 quai E. Ansermet CH-1211 Geneva 4 (Switzerland)*.

Céline Besnard - *Laboratory of Crystallography. University of Geneva, 24 quai E. Ansermet. CH-1211 Geneva 4 (Switzerland).*

Laure Guénée - *Laboratory of Crystallography. University of Geneva, 24 quai E. Ansermet. CH-1211 Geneva 4 (Switzerland).*

Notes

The authors declare no conflict of interest.

ACKNOWLEGMENTS

This work is supported through grants from the Swiss National Science Foundation (grant 200020_207313).

REFERENCES

(1) Shepherd, H. J.; Quintero, C. M.; Molnar, G.; Salmon, L.; Bousseksou, A., Luminescent Spin-Crossover Materials. In Spin-Crossover Materials: Properties and Applications, Halcrow, M. A., Ed, John Wiley & Sons, Ltd, Chichester, **2013**, 13, 347-373.

(2) Meng, Y. S.; Liu, T., Manipulating Spin Transition to Achieve Switchable Multifunctions. *Acc. Chem. Res.* **2019**, *52*, 1369-1379.

(3) Javed, M. K.; Sulaiman, A.; Yamashita, M.; Li, Z. Y., Shedding Light on Bifunctional Luminescent Spin-crossover Materials. *Coord. Chem. Rev.* **2022**, *467*, 214625.

(4) Gütlich, P.; Gaspar, A. B.; Garcia, Y., Spin State Switching in Iron Coordination Compounds. *Beilstein J. Org. Chem.* **2013**, *9*, 342-391.

(5) Kumar, K. S.; Ruben, M., Emerging Trends in Spin-crossover (SCO) Based Functional Materials and Devices. *Coord. Chem. Rev.* **2017**, *346*, 176-205.

(6) Benaicha, B.; Van Do, K.; Yangui, A.; Pirrala, N.; Lusson, A.; Sy, M.; Bouchez, G.; Fourati, H.; Gomez-Garcia, C. J.; Triki, S.; Boukheddaden, K., Interplay Between Spin-Crossover and Luminescence in a Multifunctional Single Crystal Iron(II) Complex: Towards a New Generation of Molecular Sensor. *Chem. Sci.* **2019**, *10*, 6791-6798.

(7) Bünzli, J.-C. G.; Eliseeva, S. V., Basics of Lanthanide Photophysics. In Lanthanide Luminescence: Photophysical, Analytical and Biological Aspects, Hänninen, P.; Härmä, H., Eds. Springer-Verlag: Berlin Heidelberg, **2010**; Vol. 7, pp 1-45.

(8) Bünzli, J.-C. G.; Eliseeva, S. V., Intriguing aspects of lanthanide luminescence. *Chem. Sci.* **2013**, *4*, 1939-1949.

(9) Bünzli, J.-C. G., Lanthanide Luminescence: From a Mystery to rationalization, Understanding and Applications. In *Handbook on the Physics and Chemistry of Rare Earths*, Bünzli, J.-C. G.; Pecharsky, V. K., Eds. Elsevier Science: Amsterdam, **2016**; Vol. 50, pp 141-176.

(10) Salmon, L.; Molnar, G.; Zitouni, D.; Quintero, C.; Bergaud, C.; Micheau, J. C.; Bousseksou, A., A Novel Approach for Fluorescent Thermometry and Thermal Imaging Purposes Using Spin-crossover Nanoparticles. *J. Mater. Chem. C* **2010**, *20*, 5499-5503.

(11) Kraieva, O.; Quintero, C. M.; Suleimanov, I.; Hernandez, E. M.; Lagrange, D.; Salmon, L.; Nicolazzi, W.; Molnar, G.; Bergaud, C.; Bousseksou, A., High Spatial Resolution Imaging of Transient Thermal Events Using Materials with Thermal Memory. *Small* **2016**, *12*, 6325-6331.

(12) Guo, Y. N.; Xue, S. F.; Dirtu, M. M.; Garcia, Y., A Versatile Iron(II)-Based Colorimetric Sensor for the Vapor-Phase Detection of Alcohols and Toxic Gases. *J. Mater. Chem. C* **2018**, *6*, 3895-3900.

(13) Li, H. Y.; Zhao, S. N.; Zang, S. Q.; Li, J., Functional Metal-Organic Frameworks as Effective Sensors of Gases and Volatile Compounds. *Chem. Soc. Rev.* **2020**, *49*, 6364-6401.

(14) Suleimanov, I.; Kraieva, O.; Costa, J. S.; Fritsky, I. O.; Molnar, G.; Salmon, L.; Bousseksou, A., Electronic Communication Between Fluorescent Pyrene Excimers and Spin Crossover Complexes in Nanocomposite Particles. *J Mater Chem C* **2015**, *3*, 5026-5032.

(15) Kraieva, O.; Suleimanov, I.; Molnar, G.; Salmon, L.; Bousseksou, A., CdTe Quantum Dot Fluorescence Modulation by Spin-crossover. *Magnetochemistry* **2016**, *2*, 11.

(16) Wang, J.-L.; Liu, Q.; Meng, Y.-S.; Liu, X.; Zheng, H.; Shi, Q.; Duan, C.-Y.; Liu, T., Fluorescence Modulation via Photoinduced Spin Crossover Switched Energy Transfer from Fluorophores to Fe(II) ions. *Chem. Sci.* **2018**, *9*, 2892-2897.

(17) Sun, H. Y.; Meng, Y. S.; Liu, T., Photo-Switched Magnetic Coupling in Spin-Crossover Complexes. *Chem. Commun.* **2019**, *55*, 8359-8373.

(18) Ito, A.; Meyer, T. J., The Golden Rule. Application for Fun and Profit in Electron Transfer, Energy Transfer, and Excited-State Decay. *Phys. Chem. Chem. Phys.* **2012**, *14*, 13731-13745.

(19) Beltran-Leiva, M. J.; Paez-Hernandez, D.; Arratia-Perez, R., Theoretical Determination of Energy Transfer Processes and Influence of Symmetry in Lanthanide(III) Complexes: Methodological Considerations. *Inorg. Chem.* **2018**, *57*, 5120-5132.

(20) Inokuti, M.; Hirayama, F., Influence of Energy Transfer by the Exchange Mechanism on Donor Luminescence. *J. Chem. Phys.* **1965**, *43*, 1978-1989.

(21) Tanner, P. A.; Zhou, L.; Duan, C.; Wong, K.-L., Misconceptions in Electronic Energy Transfer: Bridging the Gap Between Chemistry and Physics. *Chem. Soc. Rev.* **2018**, *47*, 5234-5265.

(22) Kong, J. T.; Shang, X. Y.; Zheng, W.; Chen, X. Y.; Tu, D. T.; Wang, M.; Song, J.; Qu, J. L., Revisiting the Luminescence Decay Kinetics of Energy Transfer Upconversion. *J. Phys. Chem. Lett.* **2020**, *11*, 3672-3680.

(23) Lathion, T.; Fürstenberg, A.; Besnard, C.; Hauser, A.; Bousseksou, A.; Piguet, C., Monitoring Fe(II) Spin-State Equilibria via Eu(III) Luminescence in Molecular Complexes: Dream or Reality? *Inorg. Chem.* **2020**, *59*, 1091-1103.

(24) Henderson, B.; Imbush, G. F., *Optical Spectroscopy of Inorganic Solids* in Monographs on the Physics and Chemistry of Materials, 44, chaps 4-9, Oxford University Press, Oxford, 2006.

(25) Blasse, G.; Gramaier, B. C., Luminescent Materials, Springer-Verlag, Berlin, pp 91-107, 1994.

(26) Förster, T., Intermolecular Energy Migration and Fluorescence. *Ann. Phys.* **1948**, *2*, 55-75.

(27) Dexter, D. L., A Theory of Sensitized Luminescence in Solids. *J. Chem. Phys.* **1953**, *21*, 836-850.

(28) Förster, T., 10th Spiers Memorial Lecture. Transfer Mechanisms of Electronic Excitation. *Discuss. Faraday Soc.* **1959**, *27*, 7-17.

(29) Hauser, A.; Enachescu, C.; Daku, M. L.; Vargas, A.; Amstutz, N., Low-Temperature Lifetimes of Metastable High-Spin States in Spin-Crossover and in Low-Spin Iron(II) Compounds: the Rule and Exceptions to the Rule. *Coord. Chem. Rev.* **2006**, *250*, 1642-1652.

(30) McCusker, J. K., Femtosecond Absorption Spectroscopy of Transition Metal Charge-Transfer Complexes. *Acc. Chem. Res.* **2003**, *36*, 876-887.

(31) Brady, C.; McGarvey, J. J.; McCusker, J. K.; Toftlund, H.; Hendrickson, D. N., Time-Resolved Relaxation Studies of Spin Crossover Systems in Solution. *Top. Curr. Chem.* **2004**, *235*, 1-22.

(32) Juban, E. A.; Smeigh, A. L.; Monat, J. E.; McCusker, J. K., Ultrafast Dynamics of Ligand-Field Excited States. *Coord. Chem. Rev.* **2006**, *250*, 1783-1791.

(33) McCusker, J. K., Electronic Structure in the Transition Metal Block and its Implications for Light Harvesting. *Science* **2019**, *363*, 484-488.

(34) Johansson, J. O., Plot Twist in the Iron Spin Saga. *Nat. Chem.* **2022**, *14*, 722-723.

(35) Malme, J. T.; Clendening, R. A.; Ash, R.; Curry, T.; Ren, T.; Vura-Weis, J., Nanosecond Metal-to-Ligand Charge-Transfer State in an Fe(II) Chromophore: Lifetime Enhancement via Nested Potentials. *J. Am. Chem. Soc.* **2023**, *145*, 6029-6034.

(36) Edder, C.; Piguet, C.; Bünzli, J.-C. G.; Hopfgartner, G., High-Spin Iron(II) as a Semitransparent Partner for Tuning Europium(III) Luminescence in Heterodimetallic d-f Complexes. *Chem. Eur. J.* **2001**, *7*, 3014-3024.

(37) Suleimanov, I.; Kraieva, O.; Molnar, G.; Salmon, L.; Bousseksou, A., Enhanced Luminescence Stability with a Tb-Spin Crossover Nanocomposite for Spin State Monitoring. *Chem. Commun.* **2015**, *51*, 15098-15101.

(38) Schäfer, B.; Bauer, T.; Faus, I.; Wolny, J. A.; Dahms, F.; Fuhr, O.; Lebedkin, S.; Wille, H.-C.; Schlage, K.; Chevalier, K.; Rupp, F.; Diller, R.; Schünemann, V.; Kapples, M. M.; Ruben, M., A Luminescent Pt2Fe Spin Crossover Complex. *Dalton Trans.* **2017**, *46*, 2289-2302.

(39) Deorukhkar, N.; Besnard, C.; Guenee, L.; Piguet, C., Tuning Spin-Crossover Transition Temperatures in Non-Symmetrical Homoleptic Meridional/Facial $[Fe(didentate)_3]^{2+}$ Complexes: What For and Who Cares About It? *Dalton Trans.* **2021**, *50*, 1206-1223.

(40) Riis-Johannessen, T.; Bernardinelli, G.; Filinchuk, Y.; Clifford, S.; Dalla Favera, N.; Piguet, C., Self-Assembly of the First Discrete 3d-4f-4f Triple-Stranded Helicate. *Inorg. Chem.* **2009**, *48*, 5512-5525.

(41) Ford, D. M., Enthalpy-Entropy Compensation is not a General Feature of Weak Association. *J. Am. Chem. Soc.* **2005**, *127*, 16167-16170.

(42) Starikov, E. B.; Norden, B., Enthalpy-Entropy Compensation: A Phantom or Something Useful? *J. Phys. Chem. B* **2007**, *111*, 14431-14435.

(43) Khakhel', O. A.; Romashko, T. P., Extrathermodynamics: Varieties of Compensation Effect. *J. Phys. Chem. A.* **2016**, *120*, 2035-2040.

(44) Kepp, K. P., Theoretical Study of Spin Crossover in 30 Iron Complexes. *Inorg. Chem.* **2016**, *55*, 2717-2727.

(45) Piguet, C., Enthalpy-Entropy Correlations as Chemical Guides to Unravel Self-Assembly Processes. *Dalton Trans.* **2011**, *40*, 8059-8071.

(46) Piguet, C.; Bünzli, J.-C. G.; Bernardinelli, G.; Hopfgartner, G.; Petoud, S.; Schaad, O., Lanthanide Podates with Predetermined Structural and Photophysical Properties: Strongly Luminescent Self-Assembled Heterodinuclear d-f Complexes with a Segmental Ligand Containing Heterocyclic Imines and Carboxamide Binding Units. *J. Am. Chem. Soc.* **1996**, *118*, 6681-6697.

(47) Aboshyan-Sorgho, L.; Lathion, T.; Guénée, L.; Besnard, C.; Piguet, C., Thermodynamic N-donor Trans Influence in Labile Pseudo-Octahedral Zinc Complexes: A Delusion? *Inorg. Chem.* **2014**, *53*, 13093-13104.

(48) Piguet, C.; Bocquet, B.; Hopfgartner, G., Syntheses of Segmental Heteroleptic Ligands for the Self-Assembly of Heteronuclear Helical Supramolecular Complexes. *Helv. Chim. Acta* **1994**, *77*, 931-942.

(49) Lathion, T.; Guénée, L.; Besnard, C.; Bousseksou, A.; Piguet, C., Deciphering the Influence of Meridional versus Facial Isomers in Spin Crossover Complexes. *Chem.. Eur. J.* **2018**, *24*, 16873-16888.

(50) Piguet, C.; Rivara-Minten, E.; Hopfgartner, G.; Bünzli, J.-C. G., Molecular Magnetism and Fe(II) spin-state Equilibrium as Structural Probe in Heterodinuclear d-f Complexes. *Helv. Chim. Acta* **1995**, *78*, 1651-1672. **L1'** is strictly identical to **L1** except for the terminal carboxamide group which is replaced with a benzimidazole unit.

(51) Brown, I. D., Recent Development in the Methods and Applications of the Bond Valence Model. *Chem. Rev.* **2009**, *109*, 6858-6919.

(52) Casanova, D.; Cirera, J.; Llunell, M.; Alemany, P.; Avnir, D.; Alvarez, S., Minimal Distortion Pathways in Polyhedral Rearrangements. *J. Am. Chem. Soc.* **2004**, *126*, 1755-1763.

(53) Alvarez, S., Polyhedra in (Inorganic) Chemistry. *Dalton Trans.* **2005**, 2209-2233.

(54) Hauser, A., Ligand Field Theoretical Considerations. *Top. Curr. Chem.* **2004**, *233*, 49-58.

(55) Evans, D. F., The Determination of the Paramagnetic Susceptibility of Substances in Solution by Nuclear Magnetic Resonance. *J. Chem. Soc.* **1959**, 2003-2005.

(56) Piguet, C., Paramagnetic susceptibility by NMR: The Solvent Correction Removed in Large Paramagnetic Molecules. *J. Chem. Educ.* **1997**, *74*, 815-816.

(57) Ostfeld, D.; Cohen, I. A., Cautionary Note on Use of Evans Method for Magnetic Measurements. *J. Chem. Educ.* **1972**, *49*, 829.

(58) England, J.; Gondhia, R.; Bigorra-Lopez, L.; Petersen, A. R.; White, A. J. P.; Britovsek, G. J. P., Towards Robust Alkane Oxidation Catalysts: Electronic Variations in Non-Heme Iron(II) Complexes and Their Effect in Catalytic Alkane Oxidation. *Dalton Trans.* **2009**, *27*, 5319-5334.

(59) Piguet, C.; Edder, C.; Rigault, S.; Bernardinelli, G.; Bünzli, J.-C. G.; Hopfgartner, G., Isolated d-f Pairs in Supramolecular Complexes with Tunable Structural and Electronic Properties. *J. Chem. Soc., Dalton Trans.* **2000**, 3999-4006.

(60) Marchi, L.; Fantuzzi, S.; Cingolani, A.; Messori, A.; Mazzoni, R.; Zacchini, S.; Cocchi, M.; Rigamonti, L., A Proficient Multivariate Approach for Iron(ii) Spin Crossover Behaviour Modelling in the Solid State. *Dalton Trans.* **2023**, *52*, 7684-7694.

(61) Piguet, C.; Bünzli, J.-C. G.; Bernardinelli, G.; Bochet, C. G.; Froidevaux, P., Design of Luminescent Building Blocks for Supramolecular Triple-Helical Lanthanide Complexes. *J. Chem. Soc., Dalton Trans.* **1995**, 83-97.

(62) Xu, S.; Smith, J. E. T.; Weber, J. M., UV Spectra of Tris(2,2'-Bipyridine)-M(II) Complex Ions in Vacuo (M = Mn, Fe, Co, Ni, Cu, Zn). *Inorg. Chem.* **2016**, *55*, 11937-11943.

(63) Sabbatini, N.; Guardigli, M.; Manet, I., Antenna Effect in Encapsulation Complexes of Lanthanide Ions. In *Handbook on the Physics and Chemistry of Rare Earths*, Gschneidner, K. A.; Eyring, L., Eds. Elsevier Science: Amsterdam, **1996**; Vol. *23*, pp 69-120.

(64) Parker, D.; Fradgley, J. D.; Wong, K. L., The Design of Responsive Luminescent Lanthanide Probes and Sensors. *Chem. Soc. Rev.* **2021**, *50*, 8193-8213.

(65) Marciniak, L.; Kniec, K.; Elzbieciak-piecka, K.; Trejgis, K.; Stefanska, J.; Dramicanin, M., Luminescence Thermometry with Transition Metal Ions. A review. *Coord. Chem. Rev.* **2022**, *469*, 214671.

(66) Hilborn, R. C., Einstein Coefficients, Cross-Sections, F Values, Dipole-Moments, and All That. *Am. J. Phys.* **1982**, *50*, 982-986.

(67) Reinhard, C.; Güdel, H. U., High-Resolution Optical Spectroscopy of $Na_3[Ln(dpa)_3]\cdot 13H_2O$ with Ln = Er, Tm, Yb. *Inorg. Chem.* **2002**, *41*, 1048-1055.

(68) M. H. V. Werts, R. T. F. Jukes, J. W. Verhoeven, *Phys. Chem. Chem. Phys.* **2002**, *4*, 1542-1548.

(69) Shavaleev, N. M.; Eliseeva, S. V.; Scopelliti, R.; Bünzli, J.-C. G., Influence of Symmetry on the Luminescence and Radiative Lifetime of Nine-Coordinate Europium Complexes. *Inorg. Chem.* **2015**, *54*, 9166-9173.

(70) Pollnau, M.; Gamelin, D. R.; Lüthi, S. R.; Güdel, H. U., Power Dependence of Upconversion Luminescence in Lanthanide and Transition-Metal-Ion Systems. *Phys. Rev.* **2000**, *B61*, 3337-3346.

(71) Zhao, G. H.; Zhang, S. H.; Yi, C.; Liu, T.; Meng, Y. S., Construction of Spin Crossover-Fluorescence Bifunctional Iron(II) Complexes with Modified Bis(pyrazole)pyridine Ligands. *New J. Chem.* **2023**, *47*, 10967-10972.

TOC Graphic